J Mater Sci: Mater Electron (2023) 34:2297

Effect of deposition potential and time substitution for $Co(OH)_2$ on controlled synthesis and electrochemical performance for electrochemical supercapacitor

Raviraja T. Patil[1], Archana S. Patil[2], Suprimkumar D. Dhas[3], Nitin B. Wadakar[1], Tushar T. Bhosale[4], and Vijay J. Fulari[1,*]

[1] *Holography and Materials Research Laboratory, Department of Physics, Shivaji University, Kolhapur 416 004, Maharashtra, India*
[2] *Department of Physics, Rajarshi Chhatrapati Shahu College, Kolhapur, Maharashtra 416 004, India*
[3] *Department of Physics, Shri Shivaji Mahavidyalaya Barshi, Barshi, Maharashtra 413 401, India*
[4] *Thin Film Nanomaterials Laboratory, Department of Physics, Shivaji University, Kolhapur, Maharashtra 416 004, India*

Received: 16 July 2023
Accepted: 6 October 2023

ABSTRACT

Interconnected nanoflakes of cobalt hydroxide $Co(OH)_2$ were deposited potentiostatically on nickel mesh (NM) at various potentials (− 0.9 V, − 1.0 V, − 1.1 V) and various times (1 min, 2 min, 3 min, 4 min, and 5 min). The FE-SEM, XRD, FT-IR, and EDS etc. studied the morphological and structural properties. The electrochemical properties evaluated in 1 M KOH electrolyte using cyclic voltammetry (CV), galvanostatic charge–discharge (GCD), and electrochemical impedance spectroscopy (EIS) techniques. The $Co(OH)_2$ nanoflakes deposited on nickel mesh with − 1.0 V for 5 min. electrode exhibits a good specific capacitance of 1035 F g^{-1}, at a current density of 1 mA cm^{-2} 1 M KOH electrolyte. In conclusion, the deposition potential and the deposition time affect the surface morphology and the electrochemical performance of the deposited $Co(OH)_2$ electrode.

1 Introduction

Supercapacitors (SCs) are the most promising and relabeled energy storage devices in today's energy consumption era; they have a high power density, fast charging and discharging, a long life cycle, and great circulation features [1–3]. The electrode material is the heart of the SCs. Electrochemical double-layer capacitors (EDLCs) based materials such as carbanions material, graphene oxides etc., and pseudo-capacitors such as conducting polymers and transition metal oxides/hydroxides (TMOs/Hs) classified based on the charge storage mechanism [4]. Various TMO/Hs like NiOH, NiO, CoOH, Co_3O_4, MnO_3, $NiCo_2O_4$ [5–10], and many TMO/Hs based composites [11], etc., have been successfully reported as electrode materials. As

Raviraja T. Patil and Suprimkumar D. Dhas have equal contributed to this work.

Address correspondence to E-mail: vijayfulari@gmail.com

https://doi.org/10.1007/s10854-023-11436-0
Published online: 13 December 2023

compared with micrometer-scale material, nanostructured material can easily handle the strain produced due to the ion insertion-desertion process. The nanostructured TMOs/Hs show good electrochemical performance [12–14]. The necessity of a flexible supercapacitor grows day by day because of wearable devices, laptops, and cell phones. Previously, various nickel mesh (NM) supported electrodes have been reported for SCs. Shinde et al. reported $NiCo_2O_4/NiCo_2S_4$ electrodes on NM for supercapacitors and demonstrated 1966 F g^{-1} specific capacitance at 5 mV s^{-1} [15]. Compatibility with different pseudocapacitive materials there are several advantages to using $Co(OH)_2$, including a definite reversible redox reaction, low cost, and environmental friendliness. Its electrochemical performance also greatly enhanced by the large interlayer spacing, which allows electrolyte ions to diffuse through the electrode. $Co(OH)_2$ has an extremely high theoretical pseudocapacitance (3460 F g^{-1}). Direct growth of active material on the current collector provides many improvements over the films that are made by using active material in the form of powder and binder such as acetylene black, N-methyl pyrrolidinone (NMP), polyvinylidene fluoride (PVDF), etc. Direct growth gives more active sites, more adherence, and more surface area in the charging-discharging process because morphology is not affected by binders. Hence, there is a need to systematically create and fabricate advanced nanostructural materials, particularly with precisely tailored structural characteristics. Over the past few years, significant efforts have been made to improve their inherent properties, such as reducing their size, coating them with conductive substrates, and introducing cationic doping on their surfaces. However, these strategies have proven somewhat inadequate when it comes to addressing the issues of severe pulverization and aggregation during electrochemical reactions. Therefore, a viable solution appears to be the direct growth of nanostructures on conductive NM substrates. Electrochemical deposition is one of the best, fastest, and most cost-effective methods for the synthesis of NSs. In electrodeposition (ED), it is very easy to control the size and growth of NSs by changing the precursor molarity, the applied voltage, the current, the potential window, the deposition timing, the working electrode etc.

The ED films show good uniformity and a high deposition rate [16–18]**.** Moreover, Electrodeposition, a traditional method for enhancing surface attributes of numerous materials, is gaining traction as a prominent way to produce nanomaterials. At present, elements like Mn, Fe, Ni, Co, and W are commonly employed in pseudocapacitor electrodes due to their significant theoretical specific capacitance. By fine-tuning their nano-scale structure and morphology, their electrochemical capabilities can be further augmented. However, their application is restricted due to challenges like low electrical conductivity, volume changes during charging/discharging, and limited ion movement in the bulk phase. To address these issues, many researchers have advocated the electrodeposition synthesis approach. Notably, a recent study by Fei Ma and colleagues unveiled that the fusion of highly conductive cobalt molybdenum sulfide with active Ni–Co–S, using electrodeposition, exhibited an impressive specific capacitance, registering 2208 F g^{-1} at a 1 A g^{-1} current density [19–21]. The cathodic ED of TMOs and Hs is more frequently reported than the anodic ED. For cathodic ED of any metal hydroxide, the metal nitrate source is usually used. It is observed that, as compared to other sources, films deposited by using a nitrate source show good nanostructured morphology. The cathodic ED of TMOs/Hs using metal nitrate sources involves the following reactions [22].

$$O_2 + 2H_2O + 4e^- \leftrightarrow 4OH^- \quad (1)$$

$$NO_3^- + 7H_2O + 8e^- \leftrightarrow NH_4^+ + 10OH^- \quad (2)$$

$$Mn^+ + nOH \leftrightarrow M(OH)n \quad (3)$$

In this study, we introduce a novel hierarchical nanoflakes-like structure composed of $Co(OH)_2$. To fabricate these nanoflakes, we employ a universal and controllable electrodeposition method. A significant aspect of this approach is the utilization of environmentally friendly cobalt nitrate and potassium nitrate to synthesize nanostructures (NSs). Subsequently, nanoflakes $Co(OH)_2$ NSs are obtained by subjecting the various electrodeposition time and potential followed by drying. As far as we know, this nanoflakes-like morphology, with active nanoparticles possesses numerous remarkable properties. Furthermore, Interconnected nanoflakes of cobalt hydroxide $Co(OH)_2$ were deposited potentiostatically on nickel mesh (NM) conductive substrates, at various potentials (− 0.9 V, − 1.0 V, − 1.1 V) and various times (1 min, 2 min, 3 min, 4 min, and 5 min), further enhancing the electrochemical performance in energy storage.

2 Experimental

2.1 Chemicals

Analytical-grade chemicals were used for the experiment cobalt (II) nitrate hexahydrate [$Co(NO_3)_2{\cdot}6H_2O$], potassium nitrate [KNO_3], and potassium hydroxide (KOH) were purchased by Thomas Baker India Pvt. Ltd. (Mumbai).

2.2 Synthesis of $Co(OH)_2$ on NM thin films

NM was cleaned ultrasonically for 15 min in distilled water. A DY2300 potentiostat was used to deposit $Co(OH)_2$ thin films on NM using the electrodeposition technique. A graphite plate was used as the counter electrode, a saturated calomel electrode (SCE) as the reference electrode, and NM was used as the working electrode in the conventional three-electrode system [23]. A thin film made of 0.1 M $Co(NO_3)_2$ and 0.1 M KNO_3 in double-distilled water at room temperature (300 K) was exposed to NM for 1 min, 2 min, 3 min, 4 min, and 5 min at constant potentials of − 0.9 V, − 1.0 V, and − 1.1 V (vs. SCE). The presence of $Co(OH)_2$ was indicated by the presence of adhesive and the uniform greenish product on the substrate. The films were rinsed in distilled water after deposition and dried at 318 K for 7 h. The mass of the deposited films was calculated by the weight difference method. The mass deposited on any current collector can be calculated theoretically by using the following formula [24].

$$m = \frac{q}{zF}M = \frac{I \times \Delta t}{zF}M \tag{4}$$

where m (gm) is mass deposited, M is the molar mass of $Co(OH)_2$, z is the ion transfer number, F is the Faraday constant, Δt is the deposition time, and I (A cm^{-1}) is the current density. The $Co(OH)_2$ films with different electrodeposition voltages were enumerated as 09, 10, and 11 for − 0.9 V, − 1.0 V, and − 1.1 V, respectively. Further films were labeled as C09-1, C09-2, C09-3, C09-4, and C09-5 for 1 min, 2 min, 3 min, 4 min, and 5 min respectively, to further differentiate the different deposition times. Similarly, films denote C10-1, C10-2, C10-3, C10-4, and C10-5 and C11-1, C11-2, C11-3, C11-4, and C11-5 for deposition potentials of − 0.9 V, − 1.0 V and − 1.1 V, respectively. The schematic for the synthesis of $Co(OH)_2$ electrode via the electrodeposition method with various parameters such as potential and deposition time is presented in Fig. 1.

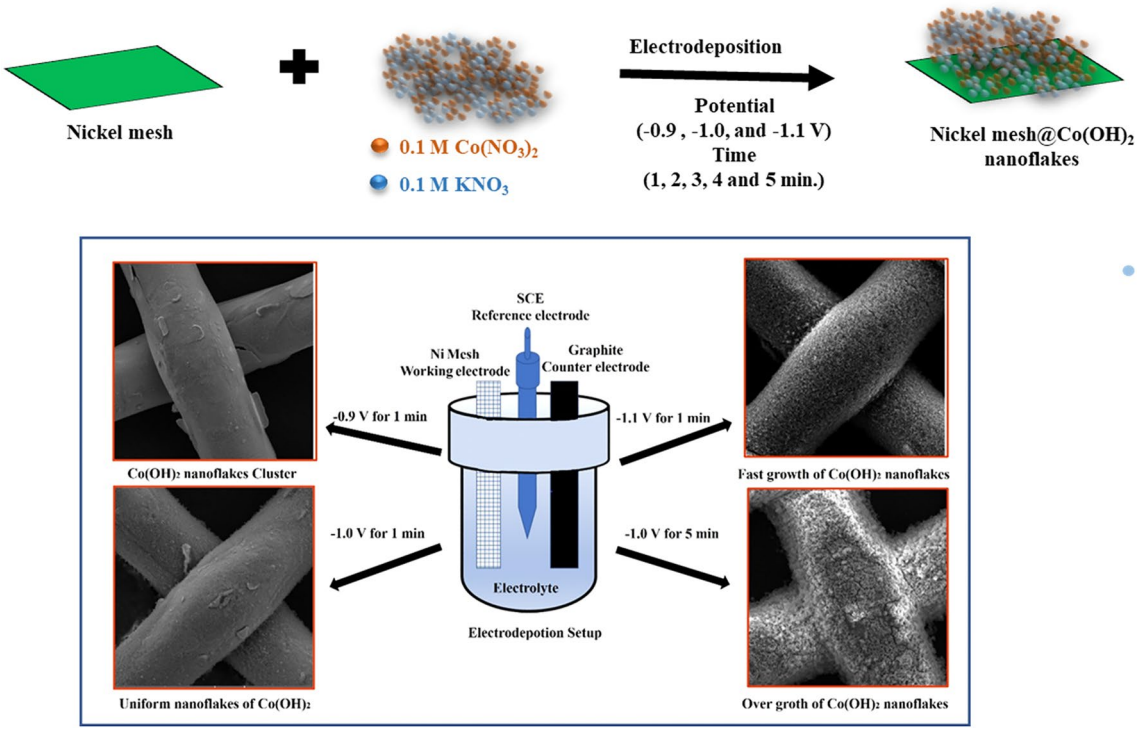

Fig. 1 Schematic of the preparation of $Co(OH)_2$ nanoflakes thin films at different deposition voltage and time

2.3 Electrodeposition mechanism

The local pH near the cathode has enhanced due to the reduction of nitrates ions when the potential applied − 0.3 V/SCE is the standard reduction potential of the nitrate ion. The reaction happened at the cathode as shown in equation (5 and 6). When potential is applied, the current rises immediately, this is due to the hydrogen evolution reaction Hydrogen reaction increases the number of the hydroxyl group and molecular hydrogen in solution [25, 26] The Co^{+2} ion combined with the $(OH)^{-2}$ ion and form a thin layer on a NM [27] the reactions are as follows,

$$2H_2O + 2e^- \rightarrow H_{2(g)} + 2OH^-_{(aq)} \quad (5)$$

$$Co^{+2}_{(aq)} + (OH)^{-2}_{(aq)} \rightarrow Co(OH)_{2(s)} \quad (6)$$

The potentiostat deposition curve Fig. 2 depicts the time-dependent changes in current density for various cathodic deposition potentials used for potentiosataic electrodeposition of $Co(OH)_2$ on Ni mesh. From the curve, it is clear that the current density decreases first due to a double-layer electric charge on the electrode surface [28] then an increase in current density indicates the formation of a well-adhered cobalt hydroxide thin film.

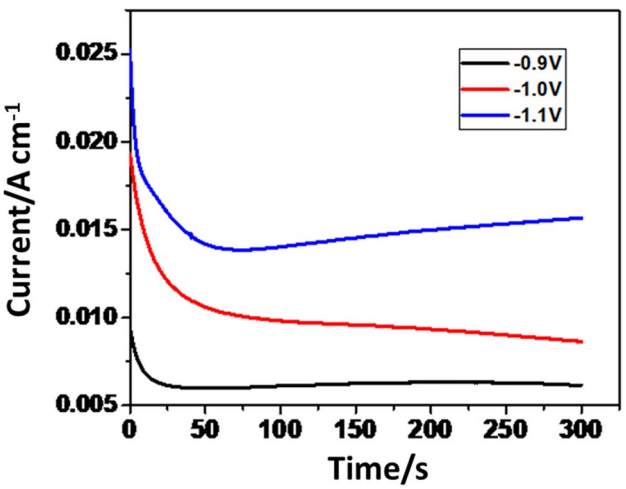

Fig. 2 The potentiostatic deposition curve of sample at − 0.9 V, − 1.0 V, and − 1.1 V for 5 min

2.4 Material characterizations

The structural properties of the thin film were investigated using an X-ray diffractometer (XRD) from a Bruker D2 phaser (tabletop model, Cu–Kα radiation = 1.54 Å), and the bonding properties of $Co(OH)_2$ were investigated using a Fourier transformation infrared spectrometer (FT-IR-4700, JASCO). The morphological properties were observed using FE-SEM (Mira-3, Tescan Pvt. Ltd.), and the energy-dispersive X-ray spectroscopy (EDS, Oxford Instruments) was used to investigate the elemental analysis.

2.5 Electrochemical measurements

The electrochemical performance of synthesized $Co(OH)_2$ on NM films was tested in an aqueous 1 M KOH solution. All electrochemical measurements such as CV, GCD, and EIS were initiated with the CH instrument (Model CHI-660-D). A three-electrode system was used, with $Co(OH)_2$ films as the working electrode, a saturated calomel electrode (SCE) as the reference electrode, and a platinum rod as a counter electrode. The EIS study was performed in the 0.1 Hz to 1 MHz frequency range at the open circuit potential (OCP).

3 Result and discussion

3.1 XRD and FT-IR study

The XRD pattern of the electrodeposited films is shown in Fig. 3a Peaks observed at 32.6°, 37.5°, 58.3°, and 89.9° correspond to $Co(OH)_2$ crystal planes. (JCPDS Card No. 02-0925) [26]. $Co(OH)_2$ nanoflakes are poorly crystallized when synthesized at room temperature [27]. Figure 3b depicts the strong absorption peaks observed in the wavenumbers 485 cm^{-1}, 487 cm^{-1}, and 490 cm^{-1} for C09-5, C10-1, and C11-1 films, respectively. This peak is observed because of Co–O–H bending and Co–O stretching vibrations. The asymmetric stretching modes between $Co(OH)_2$ and the nitrate ion are responsible for the absorption peaks observed at 1441 and 1477 cm^{-1} for C101 and C111 films, respectively. These results are well matched with the $Co(OH)_2$ nanoflowers synthesized by Wang et al., [7]. The FT-IR band position and band assignment of $Co(OH)_2$ are listed in Table 1.

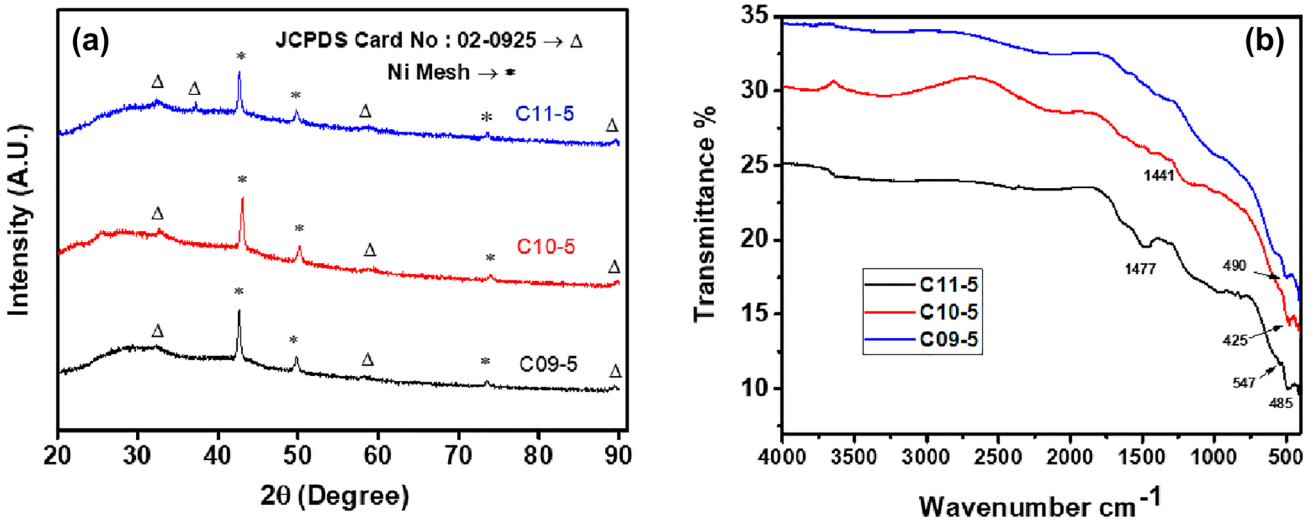

Fig. 3 **a** XRD and **b** FT-IR of C11-5, C10-5, C09-5 samples

Table 1 FT-IR band position and band assignment of Co(OH)2 nanoflakes

Sr. No.	Band position (cm^{-1})	Results
1.	425, 485, 490, 547	CO–OH stretching vibrations
3.	1441	NO^{3-} anions
4.	2525	H2O bending modes
5.	3561.6	Hydroxyl groups

3.2 Morphological and structural study

Figure 4a, c, and e show images of film deposited at − 0.9 V, − 1.0 V, and − 1.1 V for 1 min, and Fig. 4b, d, and f show FE-SEM images of film deposited at − 0.9 V, − 1.0 V, and − 1.1 V for 5 min at the magnification of ×25,000. The effect of the deposition potential observed in the FE-SEM images, as the deposition potential increases, the height of the interconnected rose petals, like nanoflakes on NM, also improves. From FE-SEM images, it is found that the thickness of nanoflakes is 80 nm. It also observed that, based on FE-SEM images, as deposition time increases, the growth of nanoflakes also increases. Only the nucleation of flakes observed at low deposition potential and short deposition time; as potential and time increased, uniform interconnected nanoflakes formed. Deposition time further increased, and interconnected nanoflakes got covered by overgrowth. Figure 5a–c show FE-SEM images of films deposited at a deposition potential of − 0.9 V (C09-1); Fig. 5d–f show a deposition potential of − 1.0 V (C10-1); and Fig. 5g–i show a deposition potential of − 1.1 V (C11-1). When compared to the other two deposition potentials, the height and length of $Co(OH)_2$ nanoflakes deposited at − 0.9 V for 1 min are very small. $Co(OH)_2$ nanoflakes grow extremely quickly and are deposited at − 1.1 V for 1 min. The interconnected and porous structure of these nanoflakes provides a large surface area for redox reactions in electrochemical supercapacitors.

3.3 The EDS study

The elements in the prepared material are confirmed by the EDS study. Figure 6a depicts the EDS graph of a $Co(OH)_2$ thin film. The graph confirms that the sample contains oxygen and cobalt in a 2:1 atomic ratio, which is consistent with the synthesis of $Co(OH)_2$. Figure 6b and c show the distribution of cobalt and oxygen uniformly distributed in the prepared material.

3.4 Electrochemical properties study

The cyclic voltammetry (CV), galvanostatic charge–discharge (GCD), and electrochemical impedance spectroscopy (EIS) measurements were used to investigate the electrochemical properties of electrodeposited $Co(OH)_2$ nanoflakes. Figure 7a, c, and e represent the CV curve performed at a 10 mV s^{-1} scan rate of $Co(OH)_2$ film deposited at − 0.9 V, − 1.0 V, and − 1.1 V for 1, 2, 3, 4, and 5 min in 1 M KOH electrolyte. Oxidation and reduction peaks clearly observed for

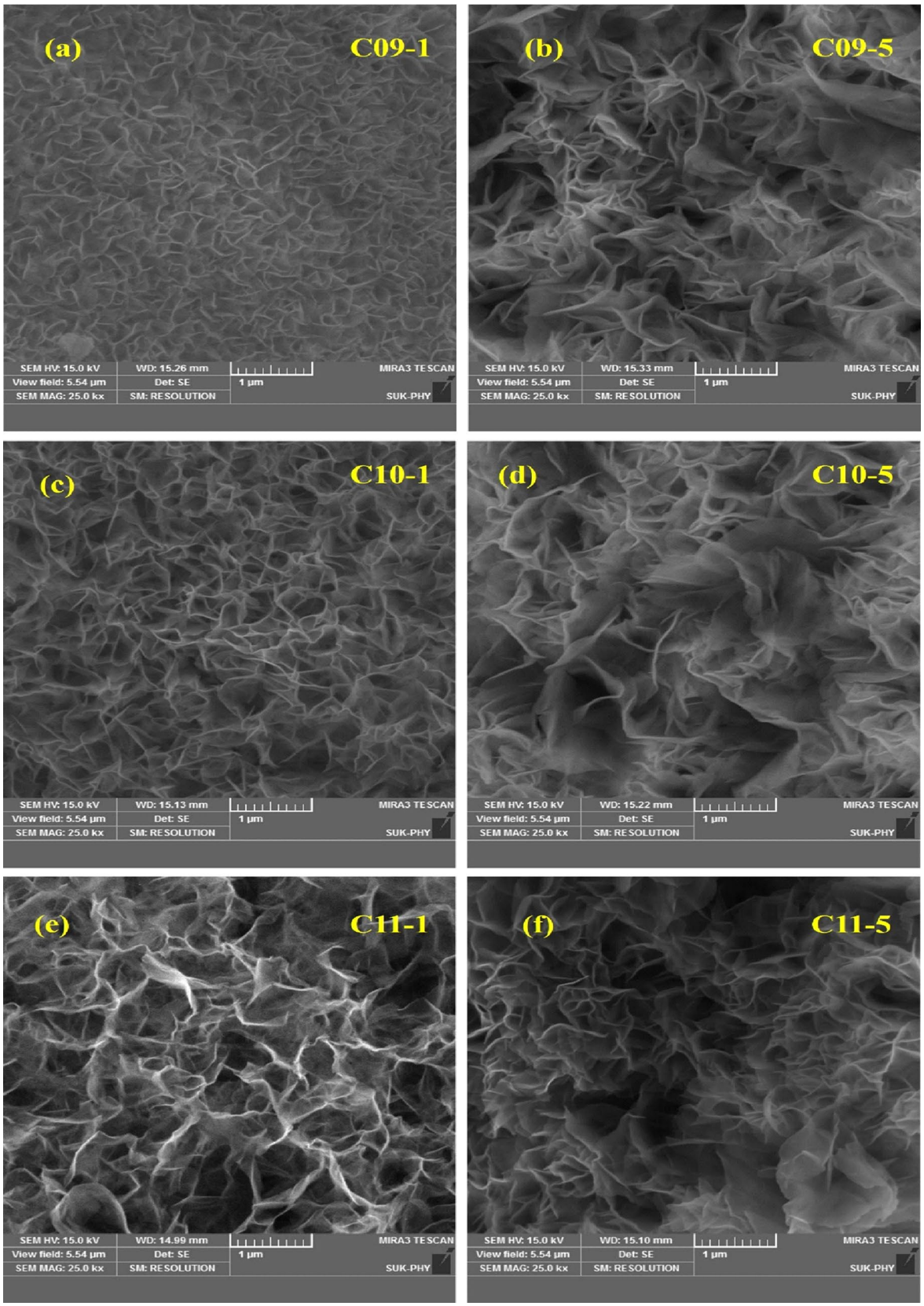

Fig. 4 The FE-SEM images of $Co(OH)_2$ of 09–5 (**a**, **b**); 10–5 (**c**, **d**) and C-11 (**e**, **f**) at 100 k×, 50 k× and 5 k× magnification

all films. During the charging and discharging processes, the following possible Faradic reactions (7) and (8) occur [29].

$$Co(OH)_2 + OH^- \leftrightarrow CoOOH + H_2O + e^- \quad (7)$$

$$CoOOH + OH^- \leftrightarrow CoO2 + H_2O + e^- \quad (8)$$

The Randles–Sevcik plot depicts the linear connection across positive and negative peak current density and (scan rate)$^{1/2}$ (Fig. 8). In essence, the number of OH^- ions migrating toward the surface of the active materials directly affects the peak current density's intensity. Thus, the linear pattern of the C10-5 nanoarray's positive peak current density in this instance is important because it demonstrates that the material offers greater OH^- ion diffusibility and permits accessibility to more surfaces even under conditions of rapid redox processing. This further illustrates that even under scenarios of higher scan rates; C10-5 multi-layered structure and extremely porous nature still offer enough surface area and room for the transport and storage of electrical energy.

The Randles Sevcik graph of the material's peak current against the scan rate and square root of scan rate of the C10-5 electrode in 1 M KOH is displayed in Fig. 8a, b. The redox reactions diffusion-controlled rate kinetics is shown by a straight line Fig. 8b. That is, the fast redox changes at the electrode were outpacing the electrolyte charge transfer. The electrolyte's diffusion rate-controlled kinetics might also be responsible for the diminution in electrochemical performance at high scan rates. The Randles–Sevcik equation represented by the formula (9) [30].

$$I_p = \left(2.69 \times 10^5\right) n^{1.5} A\, C\, D^{0.5} \upsilon^{0.5} \quad (9)$$

I_p represents the oxidation or reduction peak current (mA), n is the number of electrons transferred in the electrochemical process (n = 2), ν is the scan rate (mV s^{-1}), C_o is the concentration of charge (M), A is the surface electrode area (cm^2), and D is the diffusion coefficient (cm^2 s^{-1}). To adsorption controlled mechanics behavior between peak current and scan rate should be linear but the relationship between peak current.

I_p plotted against the square root of the scan rate, results in a straight line, with the slope being $(2.69 \times 10^5) n^{1.5}$ A C $D^{0.5} \upsilon^{0.5}$. This makes it evident that diffusivity and slope are exactly related, and therefore as diffusivity rises, so does specific capacitance.

Figure 7b, d, and f show the GCD curve for all deposited films at a current density of 1 mA cm^{-2}. The specific capacitance of the as prepared electrode calculated from the following equation [31].

$$C_{sp} = \frac{I_{dis} \times \Delta t}{\Delta m \times \Delta V} F g^{-1} \quad (10)$$

where I_{dis} is the discharging current (A), Δt is the time required to discharge (s), Δm is the mass loading on the electrode (g), and ΔV is the charging-discharging potential window. The specific capacitances calculated from the GCD curves are 516 F g^{-1}, 592 F g^{-1}, 629 F g^{-1}, 755 F g^{-1}, and 817 F g^{-1} for C09-1, C09-2, C09-3, C09-4, and C09-5 films, respectively. 374 F g^{-1}, 465 F g^{-1}, 507 F g^{-1}, 929 F g^{-1}, and 625 F g^{-1} specific capacitances calculated for the C11-1, C11-2, C11-3, C11-4, and C11-5 films. The film C10-5 demonstrated maximum specific capacitances of 1035 F g^{-1}, while the films C10-1, C10-2, C10-3, and C10-4 demonstrated specific capacitances of 525 F g^{-1}, 634 F g^{-1}, 641 F g^{-1}, and 669 F g^{-1} in 1 M KOH electrolyte. Specific capacitance vs thin films of $Co(OH)_2$ deposited by electrodeposition for the different parameters is revealed in the Fig. 9. Figure 9 shows the bar chart of the specific capacitance for all electrodes. In this plot, we can perceive the electrochemical performance of all the electrodes deposited at various voltages and times. As observed in FE-SEM images, as the deposition time increases, the interconnected nanoflakes covered due to over deposition, while for a shorter deposition time, the height and interconnection of nanoflakes are lower. The height of nanoflakes was greatest at higher deposition potentials (− 1.1 V) when compared to films deposited at − 0.9 and − 1.0 V, but the interconnections between the flakes were nonuniform. The film deposited at − 1.0 V for 5 min shows sufficient height with uniform interconnection. This morphological result is in agreement with the value found for specific capacitance from the GCD curve (Fig. 7b, d, f) for different current densities. Figure 10a and b show the CV curve of sample C10-5 at different scan rates and the GCD curve of sample C10-5 for different current densities. The improved ion diffusion and efficient electron transmission in the nanoflake arrays of C09-5, C10-5, and C11-5 have been confirmed by the EIS tests. Figure 10c illustrates the Nyquist representations for these films, with the inset showing

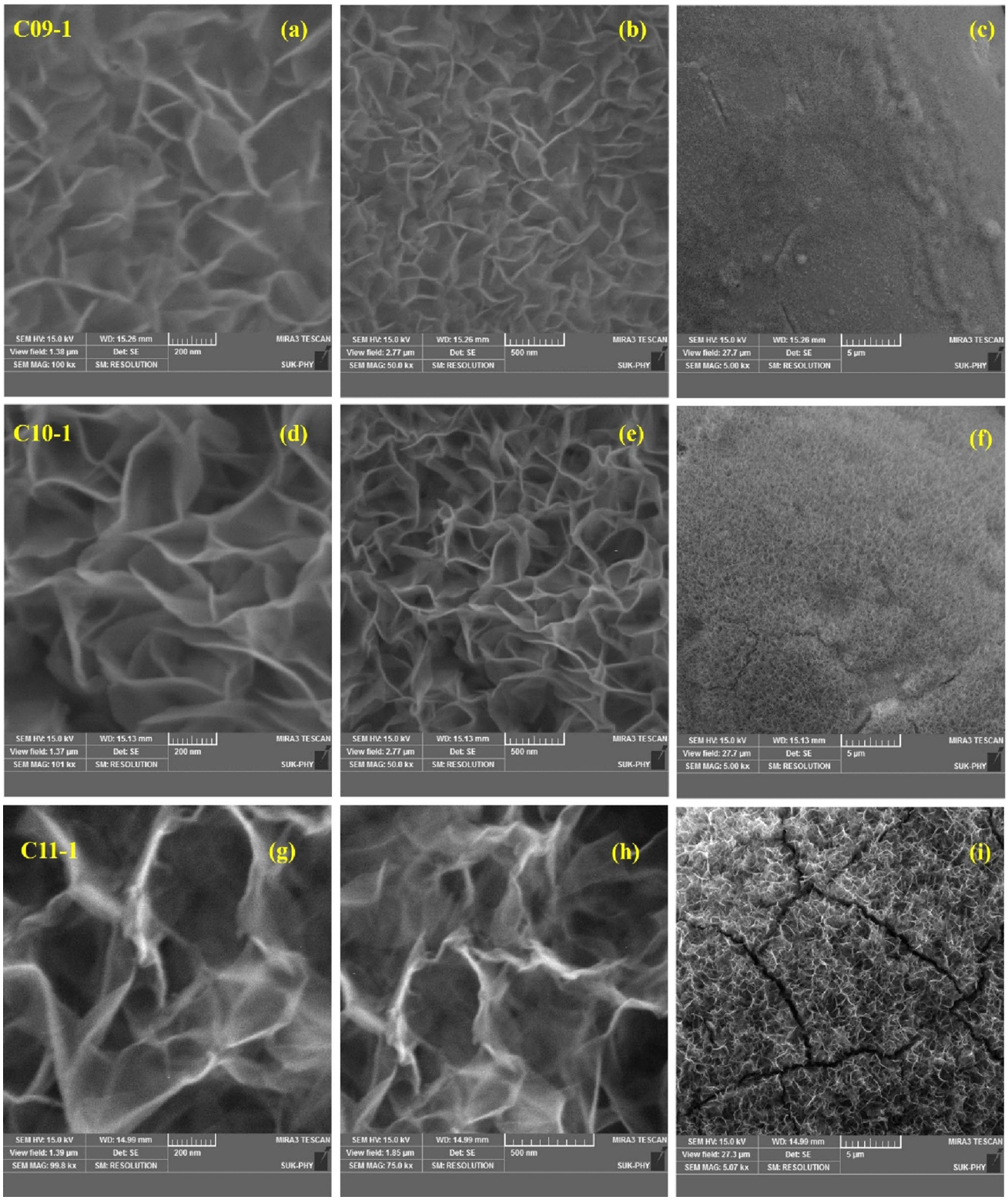

Fig. 5 The FE-SEM images of $Co(OH)_2$ of C09-1 (**a**, **b**, **c**); C10-1 (**d**, **e**, **f**) and C11-1 (**g**, **h**, **i**) at 100 k×, 50 k× and 5 k× magnifications

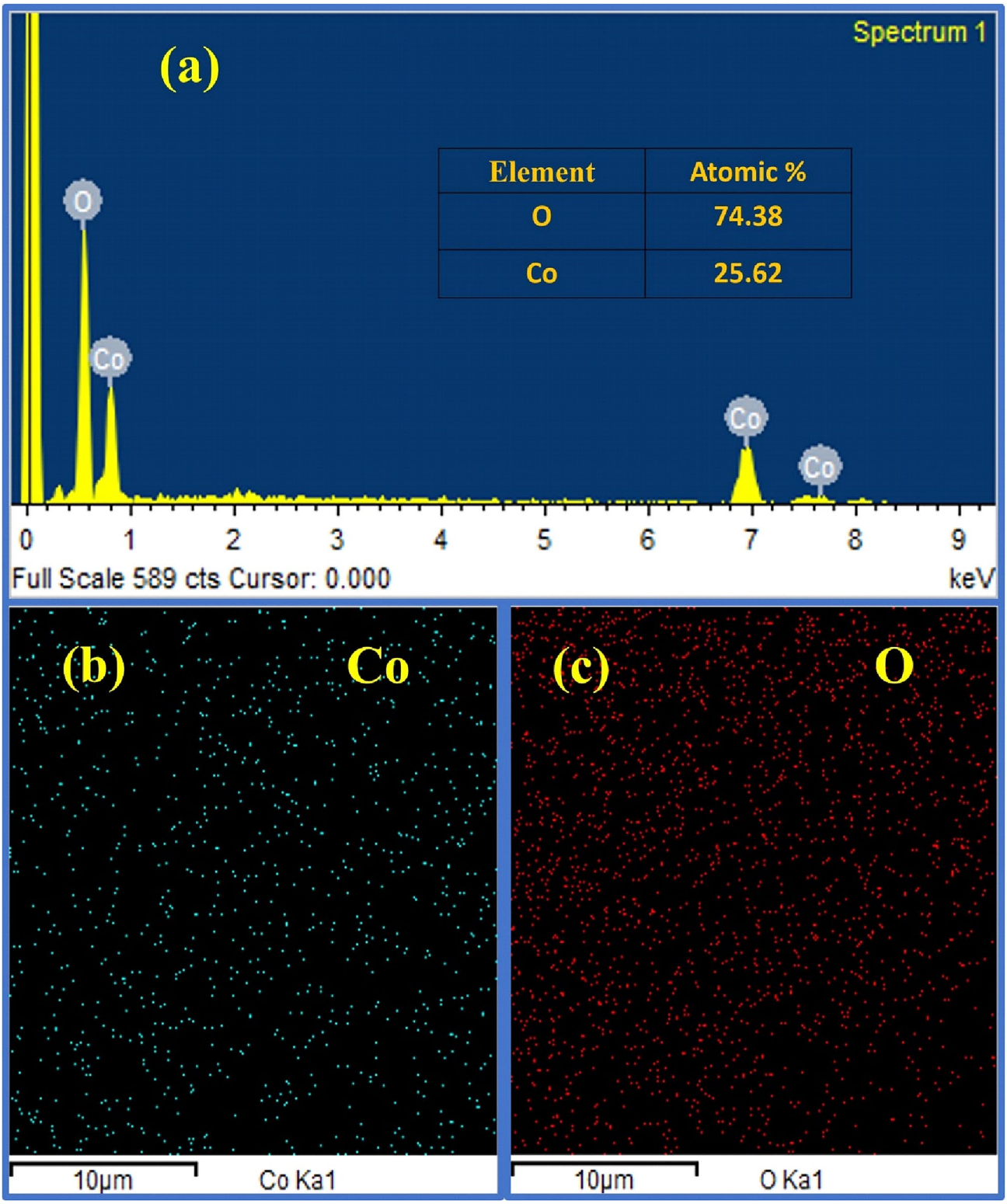

Fig. 6 **a** EDS pattern, and elemental mapping of **b** O and **c** Co of C-115 sample

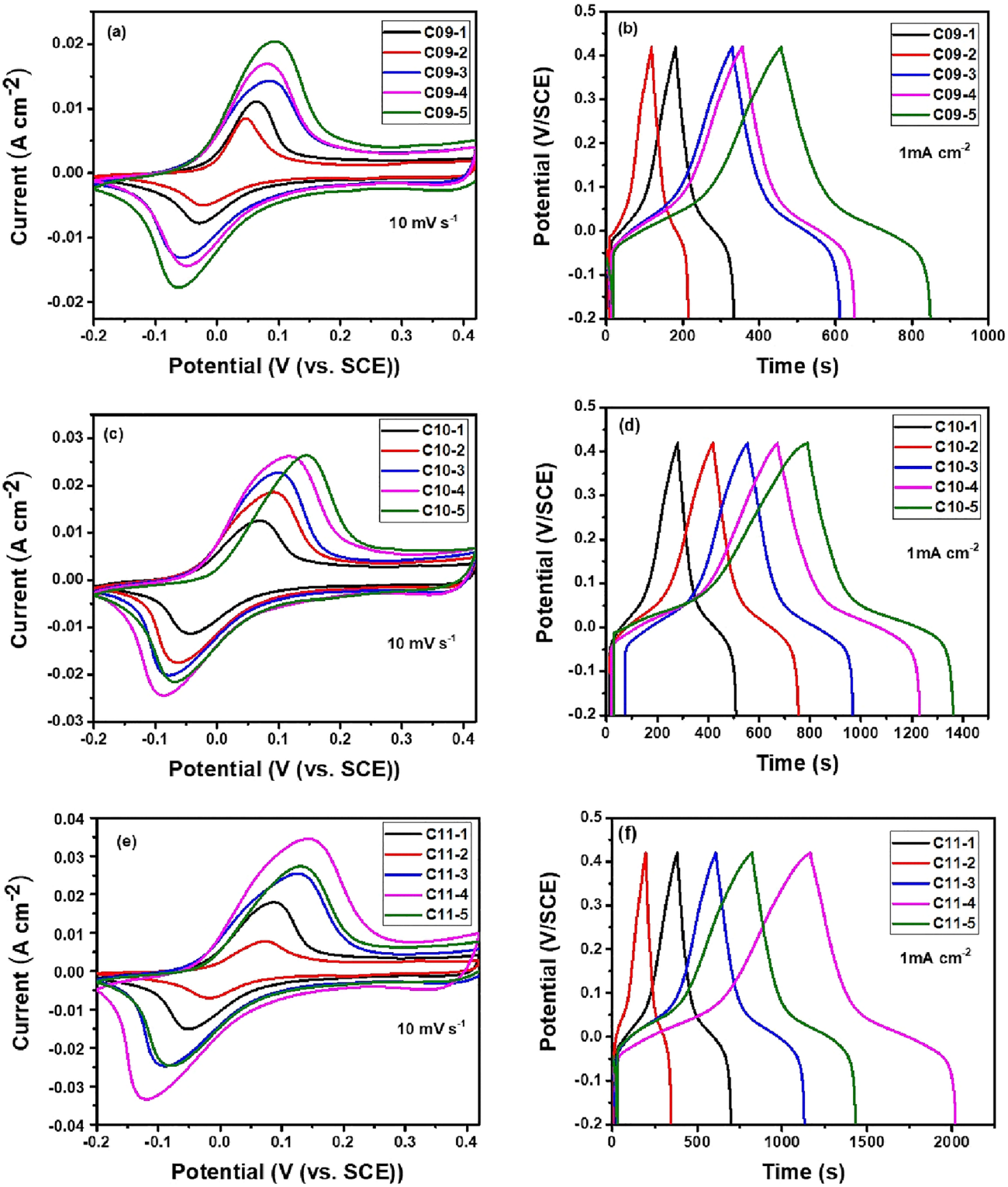

Fig. 7 **a** CV curve of sample C09-1, C09-2, C09-3, C09-4 and C09-5 at 10 mV s^{-1}, **b** GCD curves of sample C09-1, C09-2, C09-3, C09-4 and C09-5 for 1 mA cm^{-2}, **c** CV curve of sample 10-1, 10-2, 10-3, 10-4 and 10-5 at 10 mV s^{-1}, **d** GCD curves of sample 10-1, 10-2, 10-3,10-4 and 10-5 for 1 mA cm^{-2}, **e** CV curve of sample 11-1, 11-2 11-3, 11-4, 11-5 at 10 mV s^{-1}, **f** GCD curves of sample 11-1, 11-2, 11-3, 11-4 and 11-5 for 1 mA cm^{-2}

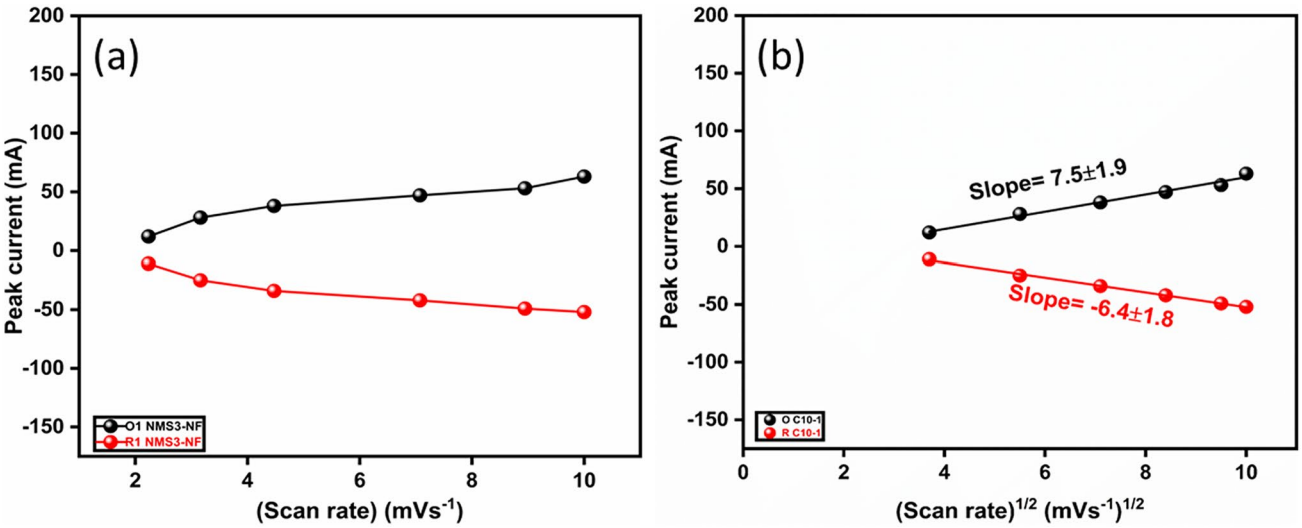

Fig. 8 **a** Plot of peak currents vs. square root of scan rate, **b** Plot of peak currents vs. scan rate of the C10-5 electrode

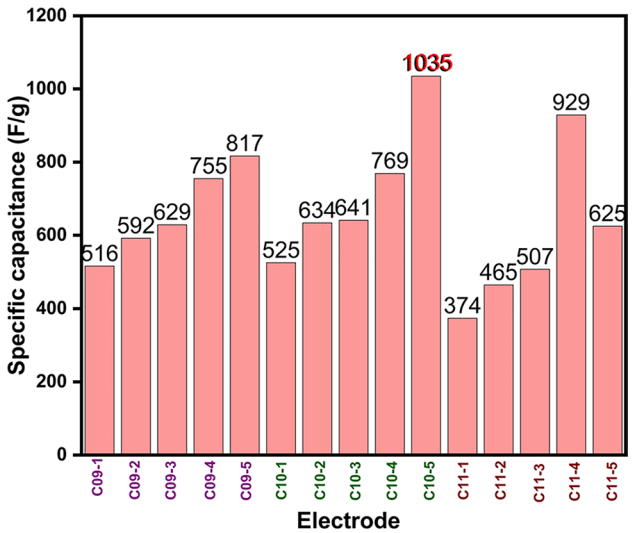

Fig. 9 Specific capacitance vs thin films of $Co(OH)_2$ deposited by electrodeposition for different parameters

the equivalent circuit for EIS of the C10-5 film. The impedance patterns for these arrays bear similarities, showing a near-semicircle in the higher frequency range and a linear segment at a lower frequency. This linear segment is associated with the Warburg impedance (W), representing the diffusion impedance of the OH– ion inside the electrode. The low-frequency linear trends for the two electrodes are nearly identical, suggesting a similar diffusion impedance in the electrolyte. Moreover, the semicircle in the Nyquist chart is linked to Faradic reactions, and its size indicates the charge-transfer impedance. The C10-5 array has a smaller charge-transfer impedance compared to C09-5 and C11-5. Measurements reveal that the C10-5's solution Rs value in 1 M KOH is 2.7 Ω, and its Rct value stands at 4.8 Ω. These findings highlight that rapid ion movement coupled with reduced electron-transfer resistance enhances the electrochemical capabilities of the C10-5 nanoflake arrays. Figure 10d shows the stability of C10-1 film after 1000 cycles with a retention of 87%.

Coulombic efficiency (η) of the prepared $Co(OH)_2$ electrodes are evaluated using Eq. (11) [32–34].

$$\eta = \frac{t_d}{t_c} \times 100 \tag{11}$$

At a current density of 1 mA cm^{-2}, the highest values of Coulombic efficiency is determined as 88.4% respectively for the Co10-1 electrode.

4 Conclusion

By applying a different potential (− 0.9 V, − 1.0 V, − 1.1 V vs. SCE) and different times (1, 2, 3, 4, 5 min) to nickel mesh, the nanoflakes of $Co(OH)_2$ have been deposited successfully. The deposited material confirmed by an XRD and EIS study. From FE-SEM images, it was observed that the growth of nanoflakes is controlled by the deposition potential value and time applied. Vertically directed mesoporous,

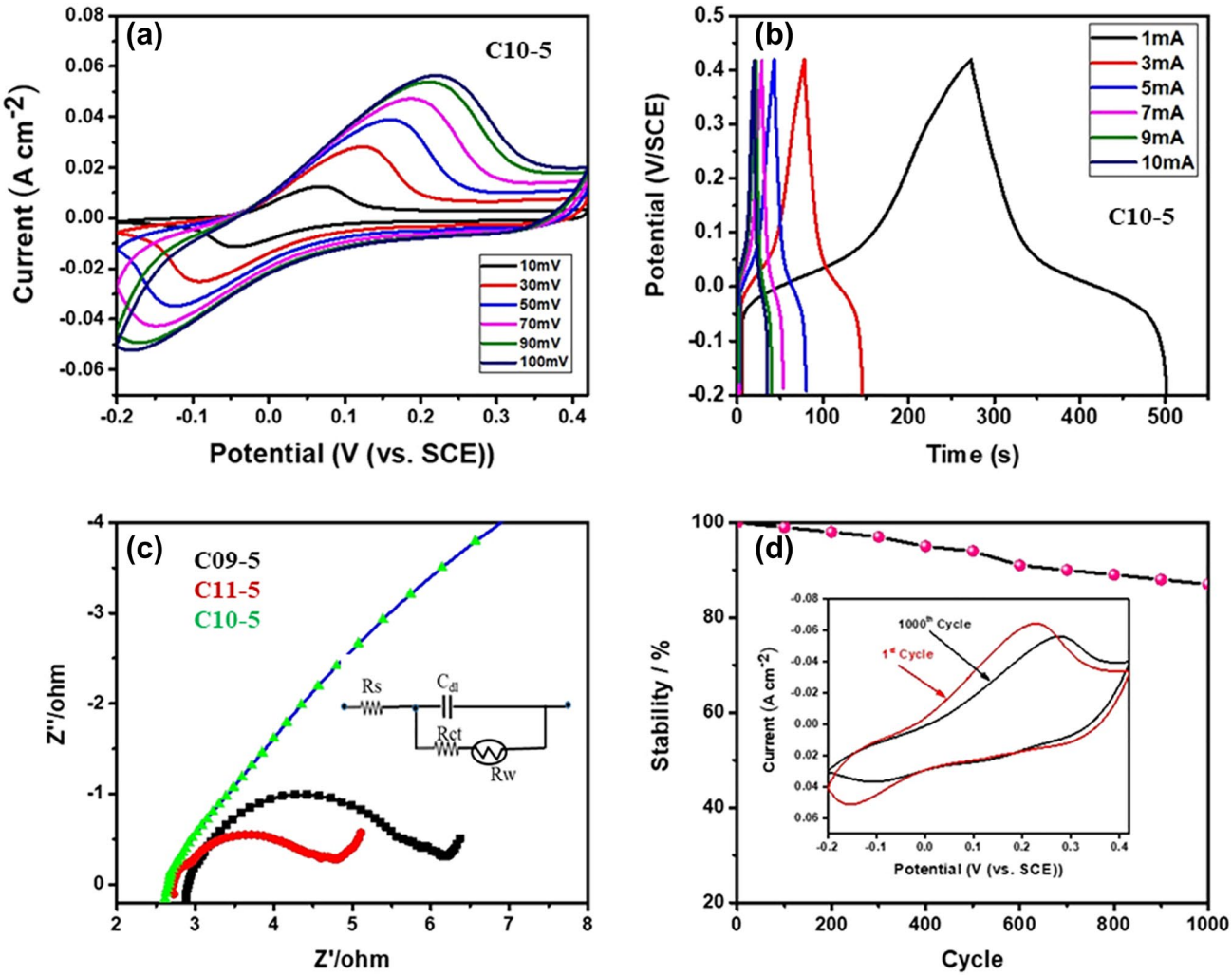

Fig. 10 **a** CV curve of sample C10-5 at different scan rates, **b** GCD curves of sample C10-5 for different current densities, **c** Nyquist plot of sample C09-5, C10-5, and C11-5, **d** Cyclic stability of C10-5 sample

interconnected nanoflakes increase the specific surface area of the electrode. The CV and GCD study in 1 M KOH shows the maximum specific capacitance of 1035 F g^{-1} for C10-5 film.

Acknowledgements

The author Dr. Suprimkumar D. Dhas is thankful to the Chhatrapati Shahu Maharaj Research Training and Human Development Institute (SARTHI), Pune, Maharashtra, for providing funding. Moreover, all the authors acknowledge the Physics Instrumentation Facility Centre (PIFC), Department of Physics, Shivaji University, Kolhapur, for characterization facilities. The financial assistance provided through DST-PURSE Phase II (2018–2022) and UGC DSA Phase II (2018–2033) is highly acknowledged.

Author contributions

RTP: Writing—Original draft preparation, Conceptualization, Supervision. ASP: Data curation, Investigation. NBW: Visualization, and Software. SDD: Editing and Resources, Conceptualization, Supervision. TTB: Validation. VJF: Funding acquisition, Writing—Review & Editing.

Funding

The authors have not disclosed any funding.

Data availability

We strive to make our research data accessible to other researchers, subject to any legal, ethical, or privacy restrictions that may apply. We will respond promptly to ensure appropriate access to the data.

Declarations

Conflict of interest The authors declare that they have no known competing financial interests or personal relationships that could have appeared to influence the work reported in this paper.

Ethical approval We recognize the importance of maintaining the confidentiality and anonymity of our research participants. All personal information and data collected during the research process are treated with utmost confidentiality. Identifiable information is stored securely and is only accessible to authorized researchers. In our publications, we ensure that individuals cannot be identified directly or indirectly, unless explicit consent has been obtained or where it is essential for the research purposes.

Informed consent We prioritize obtaining informed consent from all participants involved in our studies. Prior to their participation, we provide detailed information about the purpose of the research, procedures involved, potential risks and benefits, and any other relevant information. Participants are given the opportunity to ask questions and provide voluntary consent before their inclusion in the study. We respect the autonomy and privacy of participants, ensuring their right to withdraw from the study at any time without prejudice.

References

1. B. Xu, H. Zhang, H. Mei, D. Sun, Recent progress in metal-organic framework-based supercapacitor electrode materials. Coordin. Chem. Rev. **420**, 213438 (2020). https://doi.org/10.1016/j.ccr.2020.213438
2. F.B. Ajdari, E. Kowsari, M. Niknam Shahrak, A. Ehsani, Z. Kiaei, H. Torkzaban, M. Ershadi, S. Kholghi Eshkalak, V. Haddadi-Asl, A. Chinnappan, S. Ramakrishna, A review on the field patents and recent developments over the application of metal organic frameworks (MOFs) in supercapacitors. Coordin. Chem. Rev. **422**, 213441 (2020). https://doi.org/10.1016/j.ccr.2020.213441
3. L. Yaqoob, T. Noor, N. Iqbal, An overview of supercapacitors electrode materials based on metal organic frameworks and future perspectives. Int. J. Energy Res. **46**, 3939–3982 (2021). https://doi.org/10.1002/er.7491
4. V. Augustyn, P. Simon, B. Dunn, Pseudocapacitive oxide materials for high-rate electrochemical energy storage. Energy Environ. Sci. **7**, 1597–1614 (2014)
5. X. Yi, H. Sun, N. Robertson, C. Kirk, Nanoflower $Ni(OH)_2$ grown in situ on Ni foam for high-performance supercapacitor electrode materials. Sustain. Energy Fuels **5**, 5236 (2021). https://doi.org/10.1039/D1SE01036K
6. S.D. Dhas, P.S. Maldar, M.D. Patil, A.B. Nagare, M.R. Waikar, R.G. Sonkawade, A.V. Moholkar, Synthesis of NiO nanoparticles for supercapacitor application as an efficient electrode material. Vacuum **181**, 109646 (2020). https://doi.org/10.1016/j.vacuum.2020.109646
7. R. Wang, X. Yan, J. Lang, Z. Zhengm, P. Zhang, A hybrid supercapacitor based on flower-like $Co(OH)_2$ and urchin-like VN electrode materials. J. Mater. Chem. A **2**, 12724–12732 (2014). https://doi.org/10.1039/C4TA01296H
8. C. Park, J. Hwang, Y. Hwang, C. Song, S. Ahn, H.S. Kim, H. Ahn, Intense pulsed white light assisted fabrication of Co–CoO_x core–shell nanoflakes on graphite felt for flexible hybrid supercapacitors. Electrochim. Acta **246**, 757–765 (2017). https://doi.org/10.1016/j.electacta.2017.06.087
9. T.-F. Yi, J. Mei, B. Guan, P. Cui, S. Luo, Y. Xie, Y. Liu, Construction of spherical NiO@MnO_2 with core-shell structure obtained by depositing MnO_2 nanoparticles on NiO nanosheets for high-performance supercapacitor. Ceram. Int. **46**, 421–429 (2020). https://doi.org/10.1016/j.ceramint.2019.08.278
10. Q. Zhou, J. Xing, Y. Gao, X. Lv, Y. He, Z. Guo, Y. Li, Ordered assembly of $NiCo_2O_4$ multiple hierarchical structures for high-performance pseudocapacitors. ACS Appl. Mater. Interfaces **6**, 11394–11402 (2014). https://doi.org/10.1021/am501988s
11. Z.-S. Wu, D.-W. Wang, W. Ren, J. Zhao, G. Zhou, F. Li, H.-M. Cheng, Anchoring hydrous RuO_2 on graphene sheets for high-performance electrochemical capacitors. Adv. Funct. Mater. **20**, 3595–3602 (2010). https://doi.org/10.1002/adfm.201001054
12. N. Wang, J. He, K. Wang, Y. Zhao, T. Jiu, C. Huang, Y. Li, Graphdiyne-based materials: preparation and application for electrochemical energy storage. Adv. Mater. **31**, 1803202 (2019). https://doi.org/10.1002/adma.201803202
13. L. Miao, Z. Song, D. Zhu, L. Li, L. Gan, M. Liu, Recent advances in carbon-based supercapacitors. Mater. Adv. **1**, 945–966 (2020). https://doi.org/10.1039/D0MA00384K

14. S. Bhattacharya, I. Roy, A. Tice, C. Chapman, R. Udangawa, V. Chakrapani, J.L. Plawsky, R.J. Linhardt, High-conductivity and high-capacitance electrospun fibers for supercapacitor applications. ACS Appl. Mater. Interfaces **12**, 19369–19376 (2020). https://doi.org/10.1021/acsami
15. S.K. Shinde, M.B. Jalak, G.S. Ghodake, N.C. Maile, H.M. Yadav, A.D. Jagadale, D.S. Asif Shahzad, A.A. Lee, V.J. Kadam, D.-Y. Kim. Fulari, Flower-like $NiCo_2O_4$/$NiCo_2S_4$ electrodes on Ni mesh for higher supercapacitor applications. Ceram. Int. **45**, 17192–17203 (2019). https://doi.org/10.1016/j.ceramint.2019.05.274
16. E.M. Abebe, M. Ujihara, Simultaneous electrodeposition of ternary metal oxide nanocomposites for high-efficiency supercapacitor applications. ACS Omega **7**, 17161–17174 (2022). https://doi.org/10.1021/acsomega.2c00826
17. E. Noormohammadi, F. Poli, C. Durante, M. Lunardon, S. Sanjabi, F. Soavi, Electrodeposition of cobalt–copper oxides decorated with conductive polymer for supercapacitor electrodes with high stability. ChemElectroChem **9**(2022), e202200102 (2022). https://doi.org/10.1002/celc.202200102
18. X. Dai, M. Zhang, J. Li, Effects of electrodeposition time on a manganese dioxide supercapacitor. RSC Adv. **10**, 15860 (2020). https://doi.org/10.1039/d0ra01681k
19. F. Ma, X. Dai, J. Jin, N. Tie, Y. Dai, Hierarchical core-shell hollow CoMoS4@ Ni–Co–S nanotubes hybrid arrays as advanced electrode material for supercapacitors. Electrochim. Acta **331**, 135459 (2020)
20. M. Beidaghi, Y. Gogotsi, Capacitive energy storage in micro-scale devices: recent advances in design and fabrication of micro-supercapacitors. Energy Environ. Sci. **7**(3), 867–884 (2014)
21. H. Zhang et al., Growth of manganese oxide nanoflowers on vertically-aligned carbon nanotube arrays for high-rate electrochemical capacitive energy storage. Nano Lett. **8**(9), 2664–2668 (2008)
22. B. Xiao, W. Zhu, Z. Li, J. Zhu, X. Zhu, G. Pezzotti, Tailoring morphology of cobalt–nickel layered double hydroxide via different surfactants for high-performance supercapacitor. R. Soc. Open Sci. **5**, 180867 (2018). https://doi.org/10.1098/rsos.180867
23. N.A. Salleh, S. Kheawhom, A.A. Mohamad, Characterizations of nickel mesh and nickel foam current collectors for supercapacitor application. Arab. J. Chem. **13**, 6838–6846 (2020). https://doi.org/10.1016/j.arabjc.2020.06.036
24. N.C. Maile, S.K. Shinde, R.R. Koli, A.V. Fulari, D.Y. Kim, V.J. Fulari, Effect of different electrolytes and deposition time on the supercapacitor properties of nanoflake-like $Co(OH)_2$ electrodes. Ultrason. Sonochem. **51**, 49–57 (2019). https://doi.org/10.1016/j.ultsonch.2018.09.003
25. D. Singh, R.G. Jadhav, A.K. Das, Electrodeposition of binder-free peptide/$Co(OH)_2$ nanohybrid electrodes for solid-state symmetric supercapacitors. Energy Fuels **35**, 16152–16161 (2021). https://doi.org/10.1021/acs.energyfuels.1c01850
26. J.S. Santos, F. Trivinho-Strixino, E.C. Pereira, Investigation of $Co(OH)_2$ formation during cobalt electrodeposition using a chemometric procedure. Surf. Coat. Technol. **205**, 2585–2589 (2010). https://doi.org/10.1016/j.surfcoat.2010.10.005
27. T. Nguyen, M. Boudard, M. Carmezim et al., Layered $Ni(OH)_2$-$Co(OH)_2$ films prepared by electrodeposition as charge storage electrodes for hybrid supercapacitors. Sci. Rep. **7**, 39980 (2017). https://doi.org/10.1038/srep39980
28. S. Tang, X. Li, M. Courté, J. Peng, D. Fichou, Hierarchical $Cu(OH)_2$@$Co(OH)_2$ nanotrees for water oxidation electrolysis. ChemCatChem **20**, 4038–4043 (2020). https://doi.org/10.1002/cctc.202000558
29. V. Gupta, T. Kusahara, H. Toyama, S. Gupta, N. Miura, Potentiostatically deposited nanostructured α-$Co(OH)_2$: a high performance electrode material for redox-capacitors. Electrochem. Commun. **9**, 15–23 (2007). https://doi.org/10.1016/j.elecom.2007.06.041
30. S.D. Dhas, P.S. Maldar, M.D. Patil, S.A. Mane, M.R. Waikar, R.G. Sonkawade, A.V. Moholkar, Fabrication of efficient electrochemical capacitors rooted in sol-gel derived $NiMn_2O_4$ nanoparticles. J. Electroanal. Chem. **897**, 1572–6657 (2021). https://doi.org/10.1016/j.jelechem.2021.115548
31. S.D. Dhas, P.S. Maldar, M.D. Patil, M. Waikar, R.G. Sonkawade, S. Chakarvarti, S. Shinde, D. Kim, A. Moholkar, Probing the electrochemical properties of $NiMn_2O_4$ nanoparticles as prominent electrode materials for supercapacitor applications. Mater. Sci. Eng. B **271**, 115298 (2021). https://doi.org/10.1016/j.mseb.2021.115298
32. Y. Ma, X. Xie, W. Yang et al., Recent advances in transition metal oxides with different dimensions as electrodes for high-performance supercapacitors. Adv. Compos. Hybrid Mater. **4**, 906–924 (2021). https://doi.org/10.1007/s42114-021-00358-2
33. D. Wu, X. Xie, Y. Ma, J. Zhang, C. Hou, X. Sun, X. Yang, Y. Zhang, H. Kimura, W. Du, Morphology controlled hierarchical NiS/carbon hexahedrons derived from nitrilotriacetic acid-assembly strategy for high-performance hybrid supercapacitors. Chem. Eng. J. **433**, 133673 (2022). https://doi.org/10.1016/j.cej.2021.133673
34. V. Sunil, A. Yasin, B. Pal, I. Misnon, C. Karuppiah, C.-C. Yang, R. Jose, Tailoring the charge storability of commercial activated carbon through surface treatment. J. Energy

Storage **55**, 105809 (2022). https://doi.org/10.1016/j.est.2022.105809